Balloon-borne observations of acoustic-gravity waves from the 2022 Hunga Tonga eruption in the stratosphere

Aurélien Podglajen[1], Alexis Le Pichon[2], Raphaël F. Garcia[3], Solène Gérier[3], Christophe Millet[2], Kristopher Bedka[4], Konstantin Khlopenkov[5], Sergey Khaykin[6], Albert Hertzog[7]

[1]Laboratoire de Météorologie Dynamique (LMD/IPSL), École polytechnique, Institut polytechnique de Paris, Sorbonne Université, École normale supérieure, PSL Research University, CNRS, Paris, France
[2]CEA, DAM, DIF, 91297 Arpajon, France
[3]Institut Supérieur de l'Aéronautique et de l'Espace (ISAE-SUPAERO), Université de Toulouse, 10 Ave E. Belin 31400 Toulouse, France
[4]NASA Langley Research Center, Hampton, Virginia, USA
[5]Science Systems and Applications, Inc., Hampton, Virginia, USA
[6]Laboratoire Atmosphères, Observations Spatiales (LATMOS), UVSQ, Sorbonne Université, CNRS, IPSL, Guyancourt, France
[7]Laboratoire de Météorologie Dynamique (LMD/IPSL), Sorbonne Université, École polytechnique, Institut polytechnique de Paris, École normale supérieure, PSL Research University, CNRS, Paris, France

Key Points:

- Unique stratospheric in situ observations of the multiple revolutions of the Lamb and infrasound waves triggered by the Hunga-Tonga eruption
- Insight into eruption scenario and profile of energy release from infrasound in broad agreement with stereoscopic plume top height retrieval
- Test bed for the monitoring of infrasound generated by large explosive sources using stratospheric balloons observations

Corresponding author: Aurélien Podglajen, `aurelien.podglajen@lmd.ipsl.fr`

Abstract

The 15 January 2022 explosion of the Hunga Tonga-Hunga Ha'apai (HT-HH) volcano generated an extreme, quasi-instantaneous perturbation of the atmosphere. As part of its adjustment following the eruption, a rich spectrum of waves radiated away from HT-HH and achieved worldwide propagation. Among numerous platforms monitoring the event, two long-duration stratospheric balloons flying over the tropical Pacific provided unique observations of Lamb and infrasonic wave arrivals, detecting three revolutions of the Lamb wave and five of infrasound waves. Combined with ground measurements from the infrasound network of the International Monitoring System, such observations bring precious insights into the eruption process (chronology and altitude of energy release), and highlight previously unobserved long-range propagation of infrasound modes triggered by the eruption and their dispersion patterns. A comparison between ground- and balloon-based measurements emphasizes generally larger signal-to-noise ratios onboard the balloons and further demonstrates their potential for infrasound studies.

Plain Language Summary

The eruption of the Hunga Tonga-Hunga Ha'apai volcano on January 15 2022 was one of the most powerful blast of the last century. This fast and strong perturbation of the atmosphere triggered atmospheric waves which were followed around the world multiple times. Here, we use records of sound waves emitted by the eruption from two balloons flying at about 20 km altitude over the Pacific combined with ground stations around the volcano to help characterize the event, its scenario and its energy. Due to weak relative wind and turbulence, the sounds on the balloon are generally clearer than on the ground, demonstrating the potential of high-altitude measurements for extreme events.

1 Introduction

After a phase of mild activity started in mid-December 2021, the 2022 eruption of the Hunga Tonga-Hunga Ha'apai (HT-HH) volcano climaxed with an intense explosion on January 15th around 04:16 UTC (Poli & Shapiro, 2022). Over the next hour, the volcanic plume penetrated deep into the atmosphere, reaching the stratopause and beyond (up to 58 km), whereas the umbrella cloud spread at approximately 35 km to form a 600 km diameter disk. The altitude of volcanic overshoots, the height and extent of the umbrella cloud set a new record for volcanic eruptions over the satellite era (Carr et al., 2022), overtaking Mount Pinatubo and its 35 km. The plume generated a large perturbation of the stratospheric aerosol layer and stratospheric composition, with substantial local and global radiative impacts (Sellitto et al., 2022).

Besides triggering globally detected surface seismic waves (Poli & Shapiro, 2022) and a tsunami in the Pacific (Yuen et al., 2022; Matoza et al., 2022), the HT-HH eruption also excited atmospheric acoustic-gravity waves by injecting matter, energy and momentum deep into the atmosphere at an extremely fast rate compared to the time scale of atmospheric adjustment. A wide spectrum of waves was thus observed radiating away from the point source volcano (Matoza et al., 2022) including the edge Lamb wave (Matoza et al., 2022; Wright et al., 2022), infrasound (Matoza et al., 2022; Vergoz et al., 2022) and internal gravity waves (Watanabe et al., 2022; Wright et al., 2022; Ern et al., n.d.). The Lamb wave is a striking feature of this event. Its amplitude (> 11 hPa peak-to-peak near Tonga) and propagation pattern are in particular reminiscent of the wave trains observed following the historical 1883 Krakatoa eruption (Matoza et al., 2022).

Most observations of HT-HH waves were obtained by remote-sensing instruments or surface barometers, whereas the source extended to stratospheric altitudes at least. In this paper, we present unique measurements of acoustic-gravity wave trains directly from within the stratosphere gathered onboard two long-duration balloons flying over

the Pacific. While the instruments also recorded signals from the smaller January 13 HT-HH explosion, we focus here on analyzing Lamb and infrasound waves triggered by the main eruption on January 15. We describe the first and multiple-revolution arrivals in balloon data and ancillary satellite and ground-based observations. Then, we discuss how the waves may provide additional information on the eruptive process and the value of stratospheric infrasound observations for this and similar events.

2 Materials and Methods

2.1 Strateole-2 balloon data

In the frame of the Strateole-2 project (Haase et al., 2018), 17 superpressure balloons (SPBs) were launched from Seychelles by the French space agency (CNES) in October-December 2021. Strateole-2 SPBs are constant-volume balloons drifting following the prevailing wind and designed for flights of several months at a chosen density level between 18.5 and 21 km in the tropical upper troposphere-lower stratosphere. On January 15 2022, two SPBs remained over the tropical Pacific at about 18.5 km (TTL4) and 20.5 km above sea level (STR1, see Figure 1 a), b)). Various instruments are carried on-board the balloons; of interest for our study, all Strateole-2 payloads include the TSEN temperature and pressure sensors (Hertzog et al., 2007) and a GPS. Position and temperature are measured every 30 s, pressure every 1 s. The pressure sensor (Paroscientific Inc. Series 6000) has a sensor noise as low as 1 mPa/Hz below 1 Hz.

SPBs undergo vertical oscillations forced by atmospheric motions and modulated by the balloon's response. In order to correct for the associated pressure fluctuations, we derive the Eulerian pressure perturbation p_e by removing a background hydrostatic pressure gradient:

$$p_e = p \exp\left(\frac{g}{R_d T}\zeta'\right) - \overline{p} \tag{1}$$

where p and T are the raw pressure and temperature, $\overline{p}$ time-averaged pressure, ζ' geopotential height anomalies, $g = 9.81$ m s^{-2} and $R_d = 287$ J/K/kg the ideal gas constant for dry air. Without a high-frequency inertial measurement unit (IMU) onboard, we use solely GPS position interpolated at 1 s to compute ζ' and p_e. Performing this operation, care must be taken to properly account for any delay between pressure and position measurements, since a slight phase shift results in an imperfect canceling of the balloon neutral oscillations around 220 s (Massman, 1978; Vincent & Hertzog, 2014). Unless stated otherwise, pressure observations presented here correspond to p_e, but can be considered as p for frequencies above ∼0.02 Hz. Quality of the pressure data is sufficient to detect the energy peak of the oceanic microbarom around 0.2 Hz (Bowman & Lees, 2018). The horizontal wind components are estimated by finite-differentiating the GPS position time series, assuming that the balloons behave as perfect tracers of the flow.

2.2 Ancillary datasets

2.2.1 IMS microbarometer data

Infrasound stations from the International Monitoring system (IMS) of the Comprehensive Nuclear-Test-Ban Treaty Organization (CTBO) are arrays of microbarometers sensitive to acoustic pressure variations with a flat frequency response between 0.02 and 4 Hz. Here, we use data from 5 stations located either in the vicinity of the balloons or at distances of 2,000-4,000 km from HT-HH: IS22 (22.2°S 166.8°E, $d = 1850$ km from HT-HH), IS21 (8.9°S 140.2°W, $d = 3990$ km), IS24 (17.8°S 149.3°W, $d = 2755$ km), IS36 (44.0°S 176.5°W, $d = 2699$ km) and IS57 (33.6°N 116.5°W, $d = 8645$ km). Frequencies lower than 0.01 Hz (periods longer than 2 minutes) are recovered by deconvolving the high-pass instrumental filter, although the quality of the low-frequency pressure

signal may still be affected (Matoza et al., 2022). A thorough investigation of HT-HH Lamb and infrasound waves in IMS data is presented in Vergoz et al. (2022).

2.2.2 Geostationary satellite data

Level 1B infrared brightness temperature (BT) from the geostationary satellites GOES-17 (Eastern Pacific sector) and Himawari-8 (Western Pacific sector) at ∼2-km spatial resolution and 10-minute time resolution are also presented. In order to contextualize balloon-borne observations of the waves, we use the upper-tropospheric water vapor channel (band 8, 6.2 μm) with increased sensitivity to upper-tropospheric properties, although the waves can be observed in any infrared channel (Wright et al., 2022; Amores et al., 2022; Watanabe et al., 2022). Second-order time differentiation and a 31-pixel boxcart median filter are applied to the data in order to highlight wave-induced fluctuations and reduce the noise associated with weather systems.

We also employ stereoscopic cloud top height retrievals to infer the chronology of the eruption. These data are derived at NASA Langley using the parallax between almost-synchronized 10.3 μm-band images obtained from different viewing angles by the two satellites. For the HT-HH plume, the spatial resolution of the product is about 6 km and its vertical accuracy typically lies between 0.2-0.4 km. Further description of the retrieval method can be found in Supplementary material S1.

3 Results

3.1 First wave arrivals

3.1.1 The Lamb wave

The Lamb wave (Lamb, 1910; Taylor, 1929; Pierce & Posey, 1971; Salby, 1980) is the fastest mode excited by the eruption with a relatively constant propagation speed $c_{g\,Lamb} \simeq 317$ m/s ±5% typically (Bretherton, 1969; Pierce & Posey, 1971). After the eruption, the Lamb wave left a prominent signature in surface pressure observations around the world and in the BT of geostationary-satellite infrared channels (Amores et al., 2022; Wright et al., 2022; Watanabe et al., 2022). Figure 1 shows selected BT maps from GOES-17 on January 15. Phase lines are clearly identified at ∼06:20 UTC as concentric rings featuring a large positive temperature anomaly (0.3 K) in between two smaller negative anomalies. The distance travelled by the wave front is consistent with an emission around 04:16 UTC and the nominal propagation speed of 317 m/s (Amores et al., 2022).

The initial overpass of the Lamb wave occurs around 06:20 UTC (pressure maximum) for STR1 (Fig. 2 c)) and coincides with BT maximum. To further investigate the consistency of the waveform during early propagation, Figure 1 b) depicts pressure time series around the Lamb wave arrival time at various sensors. To compensate for geometric spreading, sonic impedance variations and the vertical structure of the mode, pressure amplitudes A in Fig. 2 c) are adjusted as follows (e.g., Pierce & Posey, 1971):

$$A_0 = A\sqrt{2\pi a \sin\left(d/a\right)\,\frac{\rho_r\, c_r}{\rho\, c}\, f\left(\frac{\overline{p}}{\overline{p}_r}\right)} \tag{2}$$

where a is the Earth radius, d the horizontal distance from HT-HH, ρ the density, c the wave phase celerity, and $f\left(\frac{\overline{p}}{\overline{p}_r}\right) = \left(\frac{\overline{p}}{\overline{p}_r}\right)^{\frac{\gamma-2}{\gamma}}$ for Lamb waves in an isothermal atmosphere, with $\gamma = \frac{C_P}{C_v} \simeq \frac{7}{5}$ the specific capacity ratio. $\rho_r = 1.2$ kg/m^3, $p_r = 1,000$ hPa and $c_r = 317$ m/s are the reference density, pressure and celerity, respectively. Equation 2 neglects attenuation through leakage, absorption, dispersion and lateral ray focusing. In Fig. 1 (c), we apply this correction to signals collected at various altitude and distance from the volcano, highlighting its validity for short to medium-range propagation. Besides pressure and temperature, the Lamb wave also has a signature in horizontal wind

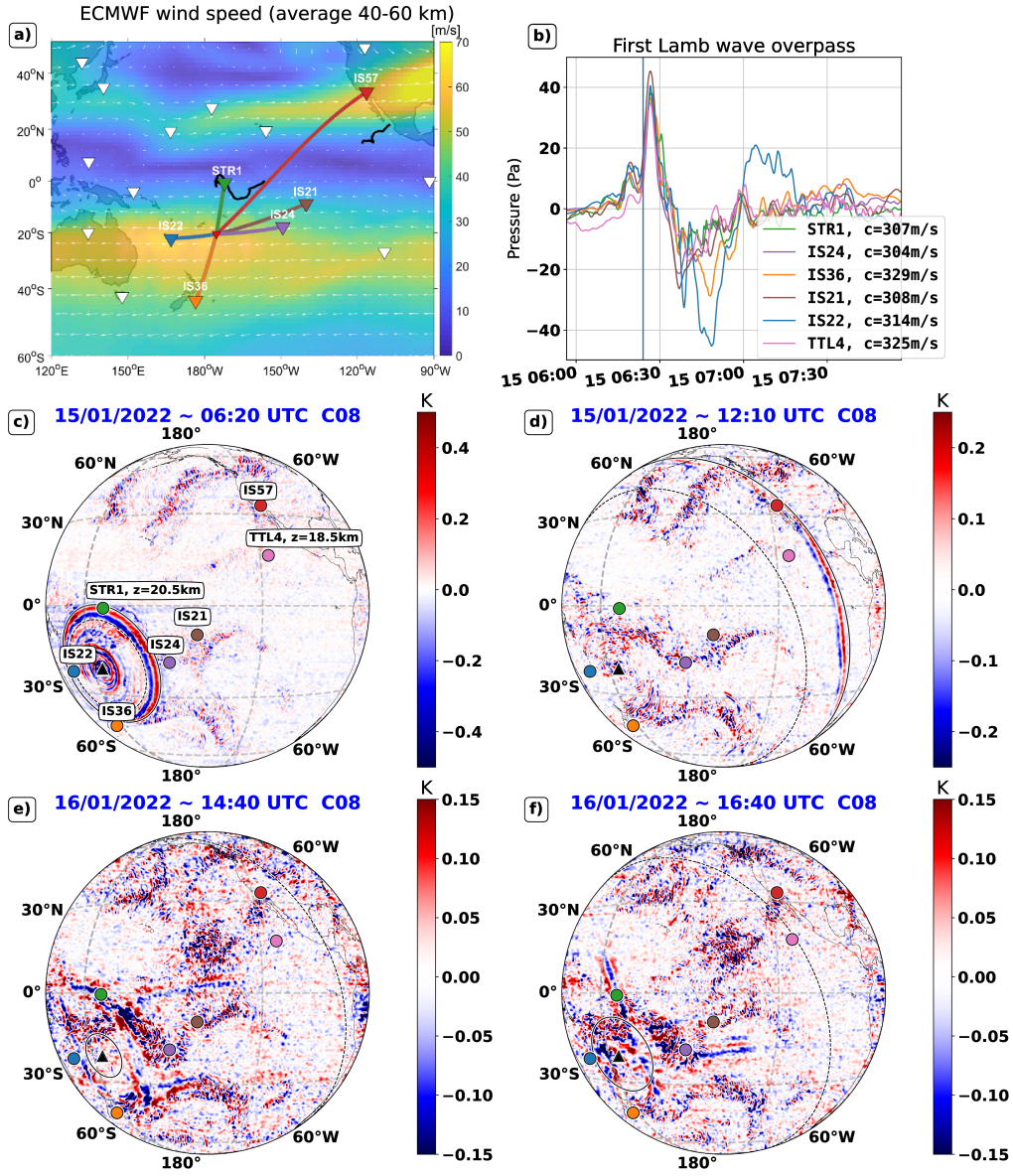

Figure 1. (a) Upper stratospheric (40-60 km average) horizontal wind direction (vectors) and speed (colors) from the European Center for Medium-range Weather Forecast (ECMWF) on January 15 2022, with ground stations and balloon trajectories (black) and (colored lines) orthodroms from HT-HH to sensor locations. (b) Lamb pressure waveforms filtered between 100 and 5,000 s. Series are aligned with respect to the time of the pressure maximum (the propagation speed c in the legend includes a ∼10 minutes delay between explosion and wave emission); pressure is adjusted to the density and pressure of STR1 using Eq. 2 for quantitative comparison. The vertical line corresponds to the time of panel (c). (c), (d), (e), (f) Selected BT images from GOES-17 band 8 (6.2 μm) showing the Lamb wave passing over STR1 (c) and the first journey and return of the Lamb wave (d, e, f). Colored dots indicate the location of the balloons and ground stations. Black circles are expected phase fronts launched from Tonga at 04:16 and propagating at 317 m/s (Lamb, solid line) or 245 m/s (dashed line).

aligned with the wave vector and in phase with pressure fluctuations, which reaches a few m/s in the lower stratosphere; although it does not stand out of the variability otherwise present, it is detected by both balloons (not shown).

Figure 2 depicts pressure spectrograms during the first overpass of the waves. The Lamb wave appears as a low-frequency pulse extending up to ~ 3 mHz. Since it is non-dispersive in the linear approximation and has limited sensitivity to refraction (Posey & Pierce, 1971), its waveform is frozen and it shows isotropic propagation during its first revolution, as evidenced by the circular wave fronts radiating away from the volcano in all directions (Fig. 1 c)) and by the similarity between the early waveforms (Fig. 1 b)). Fluctuations in the tail of the first maximum, particularly pronounced at IS22, are anisotropic (Fig. 1 a)) and due to slower modes, likely gravity waves.

3.1.2 Gravity waves

Slower gravity wave trains were observed emanating from HT-HH in geostationary and low-orbit temperature sounders (Watanabe et al., 2022; Wright et al., 2022). Those waves leave no outstanding signature in the balloon time series (raw pressure, p_e, kinetic or potential energy), in contrast with surface pressure and brightness temperature (Fig. 1 b), c)). This behavior is actually consistent with theoretical expectations for the "Pekeris mode", which predict a maximum amplitude at 4 scale heights (Salby, 1980) but a minimum at the balloons' float level (2-3 scale heights). Furthermore, while nadir-looking instruments emphasize large vertical-wavelength gravity waves, balloons have a different observational filter and also respond to shallower waves, e.g. from tropospheric convection, which contribute to mask the HT-HH gravity waves (see also Ern et al., n.d.).

3.1.3 Infrasound

Balloon-borne and surface sensors recorded at least three distinct initial infrasound wave packets (WPs, Fig. 2) above 10 mHz, separated by periods of reduced acoustic variability. On STR1, their approximate arrival times are: $t_{\mathrm{WP}_1} \simeq$ 06:35 UTC with a double peak (WP_{1a} and $\mathrm{WP1}_b \simeq$ 06:49 UTC), $t_{\mathrm{WP}_2} \simeq$ 07:18 and $t_{\mathrm{WP}_3} \simeq$ 10:38. Whereas the sub-WPs are too close in time for a definite statement, the delay between WP_1 and WP_2 is incompatible with differential propagation from a unique event with group velocities of, e.g., thermospheric and stratospheric ducts, suggesting that they are excited by distinct bursts at the source. Such hypothesis is furthermore consistent with the constant time separation between WPs at different distances from HT-HH. Back-propagating the packets to the source with $c_g \simeq 275$ m/s suggests pulses of emission around 04:19, 05:03 and 08:32. The link between this chronology and observed plume variability will be investigated later on.

Spectra at the arrival of WP_1 show a significant enhancement over the whole acoustic range compared to the period immediately prior to it (Fig. 2 a, b). The pressure variance peaks around 20-30 mHz, especially for balloon sensors . The large spread in the magnitude of the infrasound signal for the first wave packets observed among the sensors exceeds mere geometric spreading and altitude variations treated by Eq. 2, as well as the effect of dispersion. This emphasizes anisotropic infrasound propagation in particular due to the variability of along-path stratospheric winds (Fig. 1 (a)). The effect of dispersion becomes apparent at TTL4 (d=7600 km) with longer wavepackets and a duplication of WP_3.

Besides distinct WPs, balloon observations show a slow variance decrease in the acoustic range (above 0.01 Hz) and a return to pre-eruption levels after about a day. This tail of acoustic signal is analogous to the Coda observed in seismic waves (e.g. Aki, 1997) and results from wave scattering by small-scale inhomogeneities (Chunchuzov et al., 2011), e.g. related to pre-existing gravity waves.

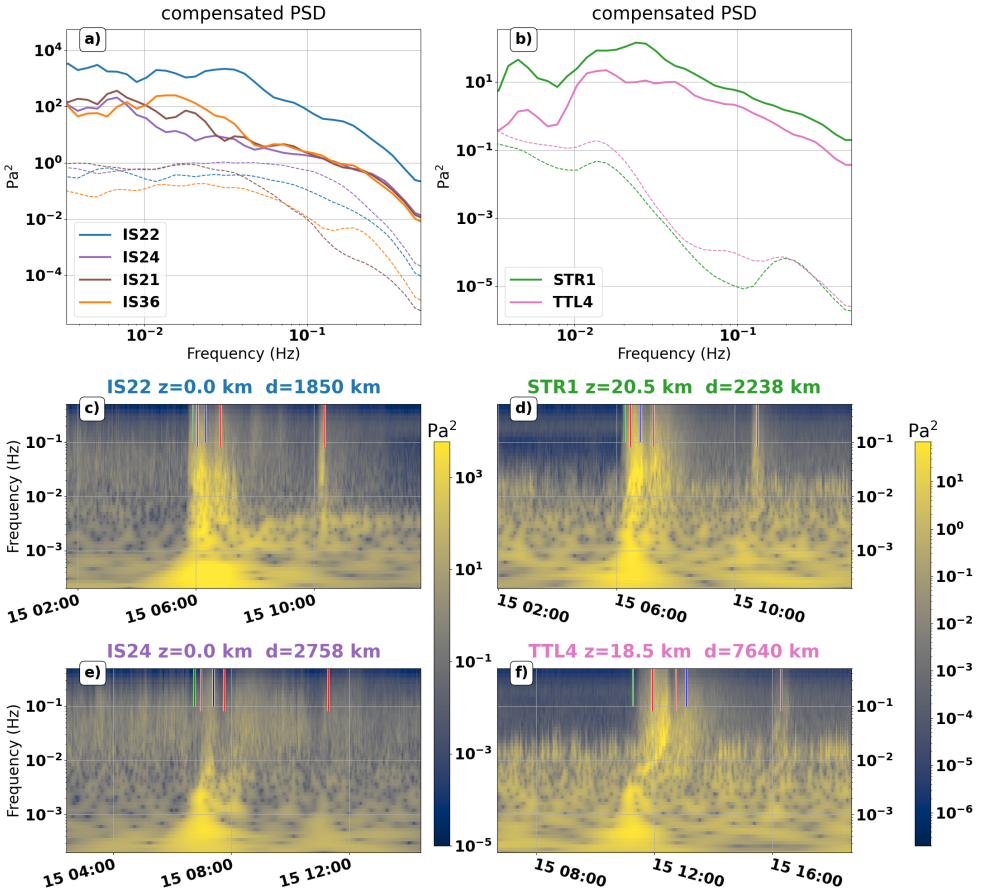

Figure 2. Compensated power spectral density (PSD multiplied by frequency) during the overpass of WP_1 (solid line) and background of the 3 hours before the eruption (dashed line) for (a) the ground stations and (b) the balloons. c), d), e), f) Selected spectrograms of the pressure signals corresponding to the first wave arrivals. The vertical lines indicate arrival times from estimated source timings (see text) and waves traveling at $c_g = 275$m/s. Blue and green line are arrival times for the first event assuming travel speed $c_g = 300$m/s and $c_g = 240$m/s, respectively.

3.2 Multiple revolutions of acoustic waves

3.2.1 Lamb wave

The HT-HH Lamb wave traveled several times around the Earth, and was detected 7 times in ground pressure measurements (Matoza et al., 2022), in agreement with its slow dissipation (Lindzen & Blake, 1972; Salby, 1980) and with observations after the 1883 Krakatoa eruption (Symons, 1888). Figure 3 shows the wavelet spectrograms of the balloon time series along with those of stations IS22 and IS57. In the low-frequency range (<3 mHz), the Lamb wave remains as a non-dispersive pulse progressively attenuated and reflected (90° phase shift) following its first transit through the antipodes (not shown).

An interesting feature of the Lamb wave at STR1 is the observation of three overpasses (instead of two) for antipodal and second transits, due to refraction by the jets and refraction-reflection by orography. This results in the emergence of straight perpendicular wavefronts (Fig. 1 (e), (f)) compared with circular wavefronts (Fig. 1 (c)). At the edge of two wavefronts, STR1 samples one more overpass than the unique expected on the second antipodal transit.

3.2.2 Infrasound

Figure 3 also emphasizes exceptional multiple passages of infrasound wavepackets. At ground stations, infrasound detections beyond the first circumnavigation are only possible under low wind conditions (Vergoz et al., 2022). Indeed, even though infrasound sensors are equipped with wind-noise reduction systems, recordings remain sensitive to atmospheric turbulences which affect the detection capability (Marty, 2019) and cause the diurnal variations of wind noise visible in Fig. 3 a), c). A clearer picture emerges from balloon observations (Fig. 3 (b), (d)), which exclusively exhibit infrasound signals above 20 mHz. In the following, we adopt the convention for multiple wave passages of Matoza et al. (2022); Vergoz et al. (2022): A1 for the direct short orthodrome arrival, A2 for the first antipodal arrival, A3 for A1 + one revolution etc.

Distinct acoustic dispersion patterns appear in long-range arrivals, some of them highlighted in Fig. 3 e)-h). Dispersion mixes A2 and A3 arrivals at STR1 (Fig. 3 e). Nevertheless, one can clearly distinguish a faster A2 wavetrain with limited dispersion ("compact mode") and typical round-the-world transit speed of 280-290 m/s, followed by a second A2 wavetrain ("dispersive mode") typically slower (275 m/s) with significant dispersion and featuring two dispersion lines around 20 mHz and 70 mHz and mixing with A3. This double dispersion line pattern is also seen for the direct arrival at station IS32 15,750 km from the source, in Kenya (Vergoz et al., 2022). The "compact mode" seems to retain the imprint of the source (i.e., distinct WP_1 and WP_2) and is visible at least up to passage A4 at STR1 (Fig. 3 f)) . The upper dispersive mode appears for passage A2 at STR1 and both A2 and A4 at TTL4. The lower dispersive line is long-lived and appears at least at A2-4 at TTL4 and A2-10 at STR1, as well as at IS22. From the spectrograms (Fig. 3 a)), we estimate $\frac{\partial c_g}{\partial \omega} \simeq 500-600$ m for the low-frequency dispersive mode. The change in travel speed with frequency results in the flattening of the WPs in frequency-time space over successive circumnavigations (Fig. 3 a)-d)).

The nature of this zoo of modes remains uncertain and will be the focus of future work. Their typical celerity resembles stratosphere-ducted infrasound with wind bringing substantial contributions in one or the other direction. Wind likely plays a role in the favored "antipodal" propagation found at TTL4 (absence of the "dispersive modes" in A3 arrivals) and the North-western American station IS56 (not shown). Such asymmetry arises due to the variable efficiency of wind ducting encountered in different propagation directions. Although balloon observations provide no information on the azimuth of the incident waves, an exceptional backazimuth drift as a consequence of refraction by the polar vortex was noted by Vergoz et al. (2022). The role of wind in supporting

specific long-lived modes and influencing propagation directions will warrant further investigations.

4 Discussion

4.1 Infrasound emission and chronology of the eruption

Distinct early infrasound WPs (Fig. 2) were attributed to consecutive trigger events at the source. In Fig. 4, time series of 0.05 Hz variance are compared with cloud top height (CTH) data. A satisfactory correspondence can be obtained using reduced time $t_r = t - \frac{d}{c}$ with $c = 275$ m/s, although we did not attempt to precisely align cloud top altitude and variance maxima or use expected azimuth-dependent celerities (Matoza et al., 2022).

Accounting for a time delay between wave emission and the plumes reaching their ceiling, a clear correspondence is found between (i) WP_1 and the first plume reaching the mesosphere (04:37) with its subsequent bursts (in particular for WP_{1b} at STR1), and (ii) WP_3 and a much later plume at 38 km altitude (08:47) piercing the umbrella cloud ($\sim$ 35 km ASL at that time). Attribution of WP_2 is less obvious: a few overshoots reach the upper stratosphere during the hour following the first injection, in contrast with 30 minutes of relative quietness between the end of WP_1 and WP_2 (t_{WP_1}+50 minutes). Nevertheless, CTH data highlights a 55 km cloud top at 05:27 (+50 minutes) surpassing smaller overshoots of the last 20 to 30 minutes. This scenario of intermittent emission broadly agrees with the chronology inferred from a ionospheric wave-train analysis by Astafyeva et al. (2022), who diagnose two explosions within 10 minutes of 4:20 UTC, followed by $\pm$ 20 minutes rest and two later explosions around 04:50. It is also broadly consistent with pressure records from Tonga at $d = 64$ km (Wright et al., 2022), although this data rather suggests four major explosions separated by 34, 41 and 175 minutes. Interpreting surface pressure records near the volcano is complicated by the entanglement between waves propagating at different speeds.

4.2 Azimuth and altitude-dependent infrasound signals: an insight on the vertical distribution of sources?

Anisotropic propagation of the infrasound is related to the stratospheric wind fields near HT-HH (Fig. 1 (a)), which imply large variations in the associated effective sound speed profiles (Fig. 4 (d)). Strong tailwinds support the propagation of stratospheric modes to IS22 (and IS36), while strong head- and crosswinds hamper it towards STR1, IS21 and IS24.

To quantify infrasound ducting and amplitude decrease along propagation paths for various source heights and source-to-receiver directions, transmission losses (T_L) between HT-HH and the sensors are calculated using the open-source range-dependent Parabolic Equation solver (NCPA PAPE, Waxler et al., 2021) with effective sound speeds profiles obtained from merging ECMWF data with climatologies above 60 km and up to 140 km (MSISE00 and HWM14, Picone et al., 2002; Drob et al., 2015), including range-dependent gravity-wave perturbations (Gardner et al., 1993). T_L are estimated in dB for a source frequency of 0.05 Hz (near the peak amplitude of WP1, Fig. 2), i.e.:

$$T_L(x,z) = 20\,\log_{10}\left(\frac{|P|^2(x,z)}{|P|^2(x=1\,\mathrm{km}, z=z_{\mathrm{source}})}\right) \tag{3}$$

where $|P|$ is the modulus of pressure amplitude, x the horizontal range from the source, z and z_{source} the observation and specified source altitudes. The resulting T_L profiles at receiver locations for different point source altitudes are depicted in Fig. 4 ((e)-(h)). A deep duct down to the surface is seen at IS22 and IS36, while the stratospheric duct prevails at other locations. Differences in T_L between IS22 and other ground and upper-

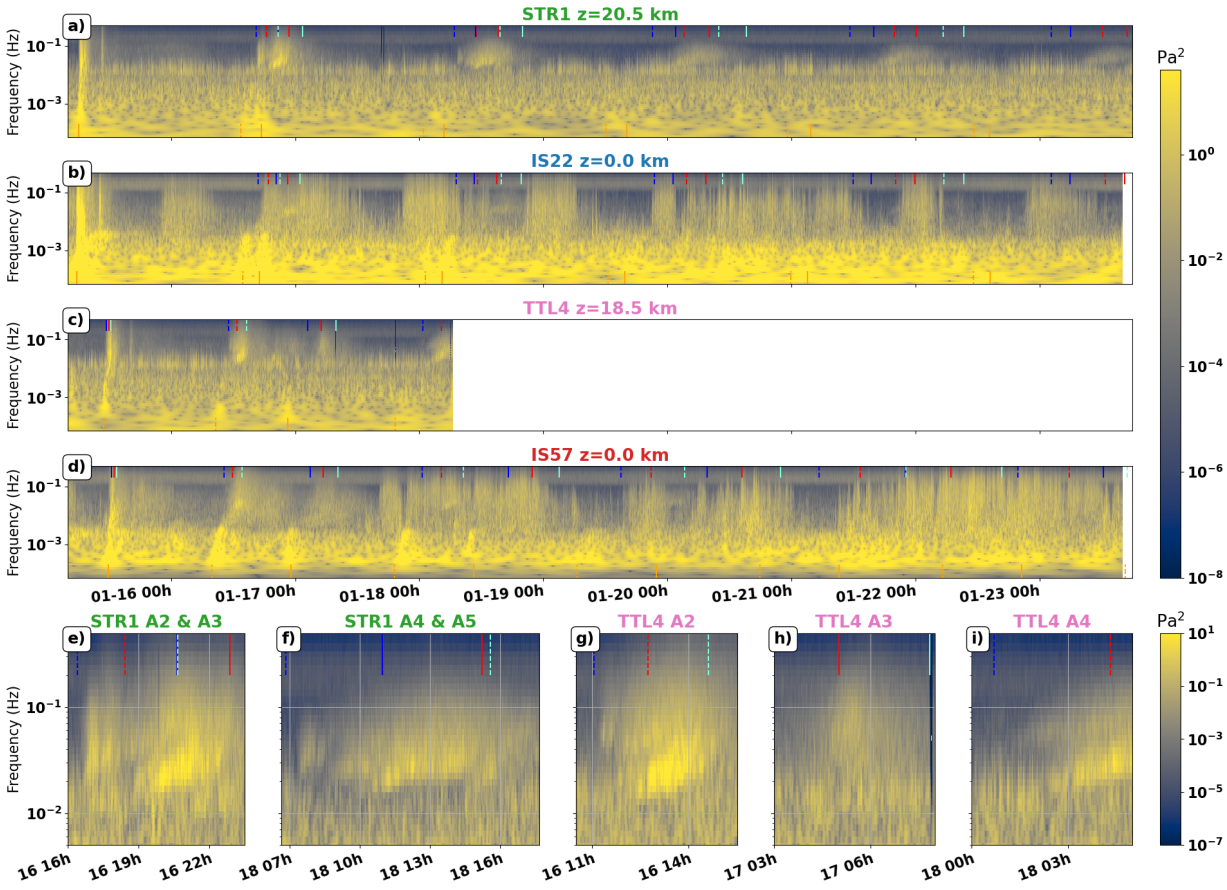

Figure 3. Spectrograms of the pressure signals corresponding to the successive circumglobal revolutions of the Lamb and infrasound wave packets for balloons a) STR1 and c) TTL4 and ground stations b) IS22 and d) IS57. Expected arrival times are shown for the 317 m/s Lamb wave (orange) and 290 (blue), 275 (red) and 260 (light green) m/s infrasound group velocities (solid lines for "direct", dashed for antipodal). TTL4 time series stop on January 18 due to its burst. e), f), g), h) Zoom on the (a, g) first antipodal arrival and (e, h) second direct and (f, i) antipodal arrivals at the balloons. Direct and antipodal arrival superpose partly at STR1.

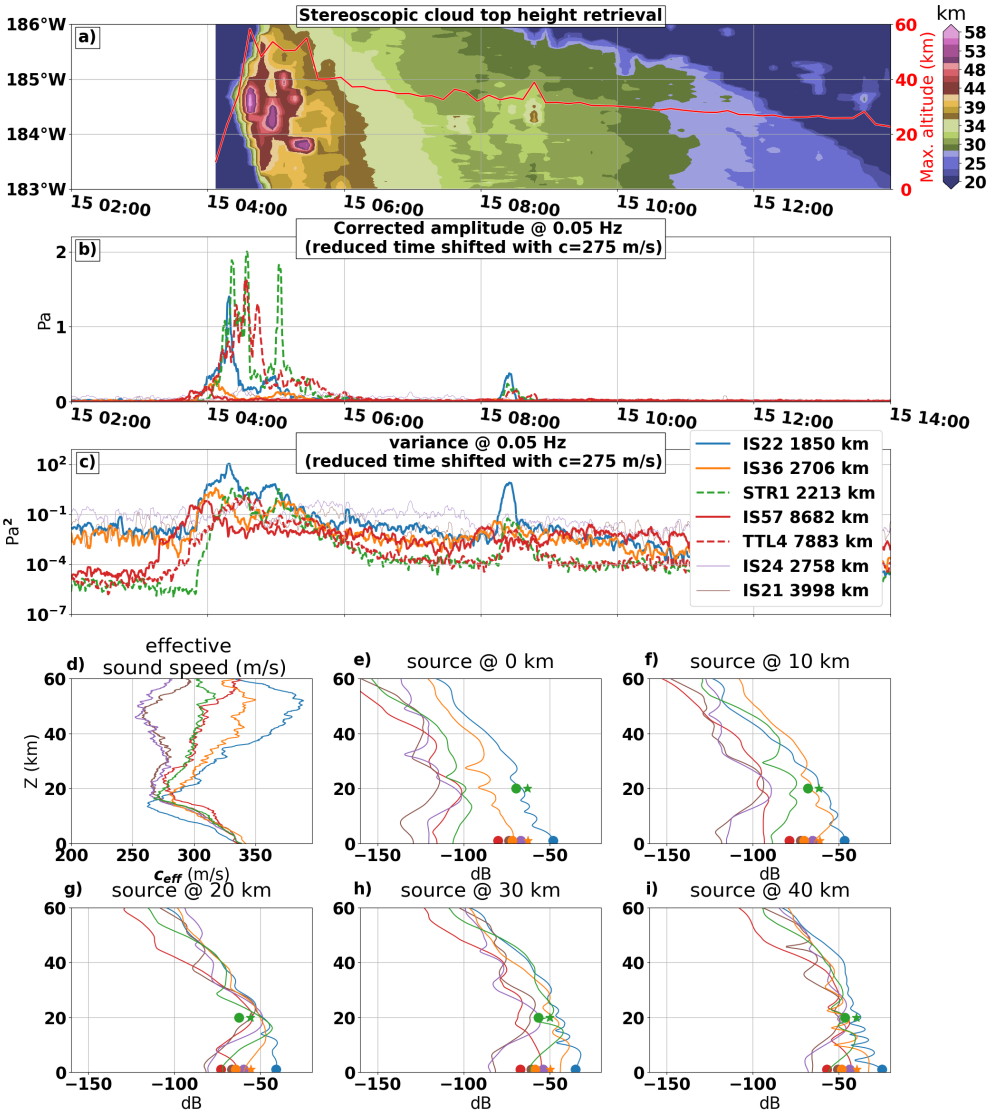

Figure 4. (a) Hovmöller diagram of HT-HH stereoscopic plume top altitude and (red line) time series of maximum plume height in the area (23°S-17°S, 177°W-174°W). (b) Amplitude time series near 0.05 Hz (4.8-5.4 10^{-2} Hz) for ground stations (solid) and balloons (dashed) corrected with Eq. 2 and (c) observed variance. (d) Average effective sound speed profile along the great-circle paths in Fig. 1 (a) $c_{eff} = \sqrt{\gamma R_d T} + \mathbf{u_h} \cdot \mathbf{e_k}$, with $\mathbf{u_h}$ the horizontal wind and $\mathbf{e_k}$ the position-dependent unit vector aligned with the orthodrom and pointing away from HT-HH. (e), (f), (g), (h) Vertical profiles of infrasound T_L at sensor position, for a source at (e) the ground, (f) 10 km altitude, (g) 20 km, (h) 30 km and (i) 40 km altitude. Star markers indicate the variance observed during WP_1 and dots during WP_3, normalized by the value at IS22.

air sensors are reduced when the altitude of the source is increased (Fig. 4 (e) vs (i)). While a quantitative Bayesian inversion is beyond the scope of the present letter, confronting the simulations to observed signals suggests that only a high-altitude (20-30 km) source can reconcile measurements from the different sensors. This is compatible with the observed plume altitude. The larger spread in magnitude at different stations for WP_3 than for WP_1 also further hints at an excitation at lower altitude for WP_3, consistent with lower top altitude in CTH retrievals. As a caveat, we should mention here that the quantitative interpretation of balloon signals might be hampered by unanticipated artifacts, e.g. related to motions of the balloon-gondola system (Garcia et al., n.d.).

In any case, assuming the Lamb wave and infrasound are excited by spatially connected processes (lightnings), a vertical distribution of energy release bears implications, e.g. for estimating the yield of the eruption. Indeed, theoretical and empirical formulas for explosion yields often assume a source primarily located at the ground (e.g., Pierce & Posey, 1971). If we relax this assumption, Equation (62) of Pierce and Posey (1971) becomes:

$$E = 15\Delta p (c_0\,\tau)^{\frac{3}{2}}\, H\, \overline{p}\, \left(\frac{\bar{p}_g}{\bar{p}_s}\right)^{\frac{2-\gamma}{\gamma}} \left(\frac{\bar{p}_{obs}}{\bar{p}_s}\right)^{-\frac{1}{\gamma}} \tag{4}$$

where H is the scale height, $\bar{p}_g$ the ground pressure, $\bar{p}_s$ the background pressure at the altitude of the point source and $\bar{p}_{obs}$ the pressure at the observations. Estimated yields are reduced by a factor of 2 (resp. 4) for a point source near 100 hPa or 16 km (resp. 10 hPa or 30 km). When evaluating their formula against nuclear blasts, Posey and Pierce (1971) questioned its applicability for extreme yield nuclear explosions. We speculate that nonlinearities in the plume evolution and high-altitude energy transfer to the environment, as well as mass and momentum sources, contribute to this discrepancy. While a detailed assessment of this effect and realistic yield estimates are beyond the scope of the present study, a significant contribution of high-altitude energy release, consistent with infrasound and geostationary observations, modify yield estimates for this event.

4.3 Advantages and potential limitations of balloon measurements

Our study evidences an infrasound signal-to-noise ratio (SNR) improved by a factor of at least 10 at lower stratospheric altitudes compared to the ground (Fig. 2 a, b and 4). Reasons include 1) the location of the sensor within the stratospheric waveguide and 2) reduced noise in the absence of wind relative to the sensor (Bowman & Lees, 2015; Bowman & Krishnamoorthy, 2021; Krishnamoorthy et al., 2020). For a source located at the surface, infrasound signals are larger on the ground in conditions favorable for deep propagation (IS22). However, upper-air reception appears advantageous in unfavorable propagation conditions (IS21, IS24, Fig. 4 (e)). In general, the strong anisotropy observed for ground receivers is mitigated at stratospheric levels. This advantage of upper-air observations is reinforced for sources around the duct (10 to 20 km ASL; Fig. 4 g)).

Regarding the noise, winds exceeding a few m/s typically result in a noise level 3 orders of magnitude larger (variance) than on-board the balloons prior to the eruption (Fig. 4). Turbulence-induced noise is a well-known challenge of ground-based infrasound monitoring (Marty, 2019). Under low surface wind (e.g. IS57) (Vergoz et al., 2022), the noise is significantly reduced and likely results in better SNR than onboard the balloon.

Despite its advantages, the balloon platform might suffer from specific biases, which could be only partially corrected by the current implementation of Eq. 1. In particular, Figure 2 showed a prominent enhancement of the stratospheric signal at 0.05 Hz absent in ground measurements. Recently, Garcia et al. (n.d.) identified a mismatch between balloon observations and pressure variations expected from infrasound generated by seismic waves after an earthquake. Those authors proposed that the observed discrepancies are induced by movements of the balloon/gondola system. Although preliminary investigations suggest that well-measured multi-revolution dispersive patterns are similar be-

tween balloon and ground measurements, detailed modeling of balloon response to incident acoustic waves is needed (Bowman et al., 2022).

5 Conclusions

A quasi-instantaneous forcing of the atmosphere occurred on January 15 2022 when Hunga Tonga-Hunga Ha'apai violently erupted. Adjustment to this cataclysmic perturbation triggered a wide spectrum of atmospheric waves unprecedented in modern observational records. Located 2,000 and 7,800 km away from the volcano, two long-duration stratospheric balloons measured a clear signature of the surface-guided Lamb wave, which produced the largest pressure perturbation ever observed at that altitude for periods between 10 and 60 minutes. Lamb wave fronts could be measured for at least 3 revolutions in the air. The eruption also excited pure acoustic waves. Supported by plume top height data, the first arrival of infrasound wave packets at frequencies of 0.05 Hz suggest a multiple-explosion eruption scenario. Later infrasound arrivals associated with multiple revolutions could be followed until the end of the flights, 9 days after the eruption, corresponding to wavepackets circumnavigating the globe 5 times.

Together with infrasound earthquake detection (Brissaud et al., 2021; Garcia et al., n.d.) and entering bolide airbust in the atmosphere (Bowman et al., 2019), this exceptional ultra long-range detection of acoustic waves from the HT-HH eruption demonstrates the potential of long-duration stratospheric balloons for quakes and explosion monitoring. A shortcoming of the 2021 Strateole-2 infrasound payload is the lack of azimuth and incidence angle measurements. Recently, different teams tried to cover this gap with inertial measurement units (IMUs) (Garcia et al., 2020; Bowman et al., 2022) or antennas of pressure sensors (Krishnamoorthy et al., 2019; Garcia et al., 2020). While Strateole-2 balloons unfortunately did not include such measurements at sufficient resolution, we advocate for including them in the future to provide additional constrain on wave and source properties. The response of SPBs to high-frequency atmospheric excitations is prone to significant uncertainties (Podglajen et al., 2016) which will be addressed in the 2024 Strateole-2 campaign by the mean of dedicated instruments. In parallel, theoretical investigations of the balloon response are required to infer atmospheric wave properties from this invaluable platform.

6 Open Research

Strateole-2 data is available at `https://data.ipsl.fr/catalog/strateole2/eng/catalog.search#/search?from=1&to=30`. Access to IMS data can be made available upon request through the virtual Data Exploitation Center at `https://www.ctbto.org/specials/vdec` (last accessed on 2022-05-11). ECMWF data can be found at `https://cds.climate.copernicus.eu/cdsapp#!/dataset/reanalysis-era5-pressure-levels?tab=form` (last accessed on 2022-05-11).

Acknowledgments

The authors thank Alain Hauchecorne and François Lott for discussions. The sponsorship of CNES, CNRS-INSU and NSF to Strateole-2 long-duration stratospheric balloon activities is gratefully acknowledged.

References

Aki, K. (1997). Seismic Coda Waves: A Stochastic Process in Earth's Lithosphere. In S. A. Molchanov & W. A. Woyczynski (Eds.), *Stochastic Models in Geosystems* (pp. 1–24). New York, NY: Springer. doi: 10.1007/978-1-4613-8500-4_1

Amores, A., Monserrat, S., Marcos, M., Argüeso, D., Villalonga, J., Jordà, G., &

Gomis, D. (2022). Numerical Simulation of Atmospheric Lamb Waves Generated by the 2022 Hunga-Tonga Volcanic Eruption. *Geophysical Research Letters*, *49*(6), e2022GL098240. doi: 10.1029/2022GL098240

Astafyeva, E., Maletckii, B., Mikesell, T. D., Munaibari, E., Ravanelli, M., Coïsson, P., ... Rolland, L. (2022, April). *The 15 January 2022 Hunga Tonga eruption history as inferred from ionospheric observations* (Preprint). Geophysics. doi: 10.1002/essoar.10511226.1

Bowman, D. C., & Krishnamoorthy, S. (2021). Infrasound From a Buried Chemical Explosion Recorded on a Balloon in the Lower Stratosphere. *Geophysical Research Letters*, *48*(21), e2021GL094861. doi: 10.1029/2021GL094861

Bowman, D. C., Krishnamoorthy, S., & Brown, P. (2019, December). Underground explosion and bolide airburst detection using balloon-borne infrasound sensors. *AGU Fall Meeting Abstracts*, *2019*, A21S-2812.

Bowman, D. C., & Lees, J. M. (2015). Infrasound in the middle stratosphere measured with a free-flying acoustic array. *Geophysical Research Letters*, *42*(22), 10,010–10,017. doi: 10.1002/2015GL066570

Bowman, D. C., & Lees, J. M. (2018). Upper Atmosphere Heating From Ocean-Generated Acoustic Wave Energy. *Geophysical Research Letters*, *45*(10), 5144–5150. doi: 10.1029/2018GL077737

Bowman, D. C., Rouse, J. W., Krishnamoorthy, S., & Silber, E. A. (2022, May). Infrasound direction of arrival determination using a balloon-borne aeroseismometer. *JASA Express Letters*, *2*(5), 054001. doi: 10.1121/10.0010378

Bretherton, F. P. (1969). Lamb waves in a nearly isothermal atmosphere. *Quarterly Journal of the Royal Meteorological Society*, *95*(406), 754–757. doi: 10.1002/qj.49709540608

Brissaud, Q., Krishnamoorthy, S., Jackson, J. M., Bowman, D. C., Komjathy, A., Cutts, J. A., ... Walsh, G. J. (2021). The First Detection of an Earthquake From a Balloon Using Its Acoustic Signature. *Geophysical Research Letters*, *48*(12), e2021GL093013. doi: 10.1029/2021GL093013

Carr, J. L., Horvath, A., Wu, D. L., & Friberg, M. D. (2022, February). *Stereo Plume Height and Motion Retrievals for the Record-Setting Hunga Tonga-Hunga Ha'apai Eruption of 15 January 2022* (Preprint). Atmospheric Sciences. doi: 10.1002/essoar.10510365.1

Chunchuzov, I. P., Kulichkov, S. N., Popov, O. E., Waxler, R., & Assink, J. (2011, October). Infrasound scattering from atmospheric anisotropic inhomogeneities. *Izvestiya, Atmospheric and Oceanic Physics*, *47*(5), 540–557. doi: 10.1134/S0001433811050045

Drob, D. P., Emmert, J. T., Meriwether, J. W., Makela, J. J., Doornbos, E., Conde, M., ... Klenzing, J. H. (2015). An update to the Horizontal Wind Model (HWM): The quiet time thermosphere. *Earth and Space Science*, *2*(7), 301–319. doi: 10.1002/2014EA000089

Ern, M., Hoffmann, L., Rhode, S., & Preusse, P. (n.d.). The Mesoscale Gravity Wave Response to the 2022 Tonga Volcanic Eruption: AIRS and MLS Satellite Observations and Source Backtracing. *Geophysical Research Letters*, *n/a*(n/a), e2022GL098626. doi: 10.1029/2022GL098626

Garcia, R. F., Klotz, A., Hertzog, A., Roland, M., Gérier, S., Kassarian, E., ... Mimoun, D. (n.d.). Infrasound from large earthquakes recorded on a network of balloons in the stratosphere.

Garcia, R. F., Martire, L., Chaigneau, Y., Cadu, A., Mimoun, D., Portus, M. B., ... Martin, R. (2020, December). An active source seismo-acoustic experiment using tethered balloons to validate instrument concepts and modelling tools for atmospheric seismology. *Geophysical Journal International*, *225*(1), 186–199. Retrieved from `https://doi.org/10.1093/gji/ggaa589` doi: 10.1093/gji/ggaa589

Gardner, C. S., Hostetler, C. A., & Franke, S. J. (1993). Gravity wave models for

the horizontal wave number spectra of atmospheric velocity and density fluctuations. *Journal of Geophysical Research: Atmospheres*, *98*(D1), 1035–1049. doi: 10.1029/92JD02051

Haase, J., Alexander, M. J., Hertzog, A., Kalnajs, L., Deshler, T., Davis, S., ... Venel, S. (2018). Around the World in 84 Days. *EOS*. doi: 10.1029/2018eo091907

Hertzog, A., Cocquerez, P., Guilbon, R., Valdivia, J.-N., Venel, S., Basdevant, C., ... Schmitt, É. (2007, December). Stratéole/Vorcore—Long-duration, Superpressure Balloons to Study the Antarctic Lower Stratosphere during the 2005 Winter. *Journal of Atmospheric and Oceanic Technology*, *24*(12), 2048–2061. doi: 10.1175/2007JTECHA948.1

Krishnamoorthy, S., Bowman, D. C., Komjathy, A., Pauken, M. T., & Cutts, J. A. (2020, October). Origin and mitigation of wind noise on balloon-borne infrasound microbarometers. *The Journal of the Acoustical Society of America*, *148*(4), 2361–2370. doi: 10.1121/10.0002356

Krishnamoorthy, S., Lai, V. H., Komjathy, A., Pauken, M. T., Cutts, J. A., Garcia, R. F., ... Cadu, A. (2019). Aerial Seismology Using Balloon-Based Barometers. *IEEE Transactions on Geoscience and Remote Sensing*, 1–11. Retrieved from `https://ieeexplore.ieee.org/document/8809415/` doi: 10.1109/TGRS.2019.2931831

Lamb, H. (1910). On atmospheric oscillations. *Proc. R. SOC. Lond.*, *A84*, 551-572.

Lindzen, R. S., & Blake, D. (1972). Lamb waves in the presence of realistic distributions of temperature and dissipation. *Journal of Geophysical Research (1896-1977)*, *77*(12), 2166–2176. doi: 10.1029/JC077i012p02166

Marty, J. (2019). The IMS infrasound network: Current status and technological developments. In A. Le Pichon, E. Blanc, & A. Hauchecorne (Eds.), *Infrasound monitoring for atmospheric studies: Challenges in middle atmosphere dynamics and societal benefits* (pp. 3–62). Cham: Springer International Publishing. doi: 10.1007/978-3-319-75140-5_1

Massman, W. J. (1978, September). On the Nature of Vertical Oscillations of Constant Volume Balloons. *Journal of Applied Meteorology*, *17*(9), 1351–1356. doi: 10.1175/1520-0450(1978)017⟨1351:OTNOVO⟩2.0.CO;2

Matoza, R. S., Fee, D., Assink, J. D., Iezzi, A. M., Green, D. N., Kim, K., ... Wilson, D. C. (2022). Atmospheric waves and global seismoacoustic observations of the january 2022 hunga eruption, tonga. *Science*, *0*(0), eeeeeeeeeee. Retrieved from `https://www.science.org/doi/abs/10.1126/science.abo7063` doi: 10.1126/science.abo7063

Picone, J. M., Hedin, A. E., Drob, D. P., & Aikin, A. C. (2002). NRLMSISE-00 empirical model of the atmosphere: Statistical comparisons and scientific issues. *Journal of Geophysical Research: Space Physics*, *107*(A12), SIA 15-1-SIA 15-16. doi: 10.1029/2002JA009430

Pierce, A. D., & Posey, J. W. (1971, December). Theory of the Excitation and Propagation of Lamb's Atmospheric Edge Mode from Nuclear Explosions. *Geophysical Journal International*, *26*(1-4), 341–368. doi: 10.1111/j.1365-246X.1971.tb03406.x

Podglajen, A., Hertzog, A., Plougonven, R., & Legras, B. (2016). Lagrangian temperature and vertical velocity fluctuations due to gravity waves in the lower stratosphere. *Geophysical Research Letters*, *43*(7), 3543–3553. doi: 10.1002/2016GL068148

Poli, P., & Shapiro, N. M. (2022, February). *Rapid characterization of large volcanic eruptions: Measuring the impulse of the Hunga Tonga explosion from teleseismic waves* (Preprint). Geophysics. doi: 10.1002/essoar.10510358.1

Posey, J. W., & Pierce, A. D. (1971, July). Estimation of Nuclear Explosion Energies from Microbarograph Records. *Nature*, *232*(5308), 253–253. doi: 10.1038/232253a0

Salby, M. L. (1980, October). The Influence of Realistic Dissipation on Planetary Normal Structures. *Journal of the Atmospheric Sciences*, *37*(10), 2186–2199. doi: 10.1175/1520-0469(1980)037⟨2186:TIORDO⟩2.0.CO;2

Sellitto, P., Podglajen, A., Belhadji, R., Boichu, M., Carboni, E., Cuesta, J., ... Legras, B. (2022). *The unexpected radiative impact of the Hunga Tonga eruption of January 15th, 202.* doi: 10.21203/rs.3.rs-1562573/v1

Symons, G. J. (1888). *The eruption of krakatoa, and subsequent phenomena: Report of the krakatoa committee of the royal society.* Wiley Online Library.

Taylor, G. I. (1929, December). Waves and tides in the atmosphere. *Proceedings of the Royal Society of London. Series A, Containing Papers of a Mathematical and Physical Character*, *126*(800), 169–183. doi: 10.1098/rspa.1929.0213

Vergoz, J., Hupe, P., Listowski, C., Le Pichon, A., & Garcés, M. e. a. (2022). A global analysis of infrasound and acoustic-gravity waves produced by the january 2022 volcanic eruption of hunga, tonga. *Earth and Planetary Science Letters, in press*.

Vincent, R. A., & Hertzog, A. (2014, April). The response of superpressure balloons to gravity wave motions. *Atmospheric Measurement Techniques*, *7*(4), 1043–1055. doi: 10.5194/amt-7-1043-2014

Watanabe, S., Hamilton, K., Sakazaki, T., & Nakano, M. (2022, March). *First Detection of the Pekeris Internal Global Atmospheric Resonance: Evidence from the 2022 Tonga Eruption and from Global Reanalysis Data* (Preprint). Atmospheric Sciences. doi: 10.1002/essoar.10510971.1

Waxler, R., Hetzer, C., Assink, J., & Velea, D. (2021, September). *Chetzer-ncpa/ncpaprop-release: NCPAprop v2.1.0.* Zenodo. doi: 10.5281/zenodo.5562713

Wright, C., Hindley, N., Alexander, M. J., Barlow, M., Hoffmann, L., Mitchell, C., ... Yue, J. (2022, March). *Tonga eruption triggered waves propagating globally from surface to edge of space* (Preprint). Atmospheric Sciences. doi: 10.1002/essoar.10510674.1

Yuen, D. A., Scruggs, M. A., Spera, F. J., Zheng, Y., Hu, H., McNutt, S. R., ... Tanioka, Y. (2022, March). Under the Surface: Pressure-Induced Planetary-Scale Waves, Volcanic Lightning, and Gaseous Clouds Caused by the Submarine Eruption of Hunga Tonga-Hunga Ha'apai Volcano Provide an Excellent Research Opportunity. *Earthquake Research Advances*, 100134. doi: 10.1016/j.eqrea.2022.100134